International Journal of Solids and Structures 143 (2018) 262–273

Contents lists available at ScienceDirect

International Journal of Solids and Structures

journal homepage: www.elsevier.com/locate/ijsolstr

Topology optimization of dielectric elastomers for wide tunable band gaps

Eliana Bortot[a,1], Oded Amir[b], Gal Shmuel[a,*]

[a] Faculty of Mechanical Engineering, Technion—Israel Institute of Technology, Haifa 32000, Israel
[b] Faculty of Civil Engineering, Technion—Israel Institute of Technology, Haifa 32000, Israel

ARTICLE INFO

Article history:
Received 15 November 2017
Revised 5 February 2018
Available online 27 March 2018

Keywords:
Dielectric elastomer composite
Tunability
Phononic crystal
Topology optimization
Band gap
Finite deformation
Wave propagation

ABSTRACT

Dielectric elastomer composites exhibit band gaps—ranges of frequencies at which elastic waves cannot propagate—that are tunable by electrostatically-controlled deformations. We show how topology optimization of such composites can widen these gaps and improve their tunability. Our case study focuses on anti-plane shear waves in fiber composites, across a designated frequency range. Employing a genetic algorithm approach, we maximize the gap width when the composite is actuated by prescribed electric fields, as well the relative change in the gap width with respect to an unactuated composite. We present optimization results for a composite whose constituents agree with commercial products. We compare these results with the performance of a composite of the same constituents arranged in circular fibers, to demonstrate the improvement achieved by the optimization. We expect that the performance of dielectric elastomer composites can be further improved, by employing a larger design space than the exemplary space in this study.

1. Introduction

The propagation of elastic waves in periodic structures is frequency dependent. Importantly, at certain frequency bands, the way in which waves scatter and interfere results with the annihilation of their propagation (Sigalas and Economou, 1992; Kushwaha et al., 1993; Hussein et al., 2014). Based on this *band gap* phenomenon, different applications with the objective to filter undesired mechanical motions, such as vibration isolators and noise suppressors, were suggested (Wen et al., 2005; Hussein et al., 2007; Yin et al., 2015). It follows that the resultant *band diagram* can be employed not only to filter waves, but also to direct their propagation (Srivastava, 2016; Zelhofer and Kochmann, 2017; Celli et al., 2017).

Structures of *tunable* band diagrams are advantageous, as their frequency range can be adapted for different objectives. The emergence of *active* structures, capable of changing their properties upon activation, opened a new avenue to achieve such tunability. Activation methods include mechanical (Babaee et al., 2016; Shmuel and Band, 2016), thermal (Ruzzene and Baz, 1999), magnetic (Bayat and Gordaninejad, 2015) and electrical means (Degraeve et al., 2015).

A promising class of electrically tunable structures is based on *dielectric elastomers,* favorable owing to their low cost, light weight, fast response, and capability to undergo large formations over 100% (Pelrine et al., 2000; Carpi et al., 2008), where recent experimental works show that under certain settings, area strains of hundreds of percents are accessible (Huang et al., 2012; Li et al., 2013; Godaba et al., 2014). Indeed, it was theoretically demonstrated that by subjecting dielectric elastomer composites to quasi-static large deformations, the band diagram of superposed waves is electrostatically tunable (Gei et al., 2011; Shmuel and Pernas-Salomón, 2016; Getz et al., 2017; Bortot and Shmuel, 2017; Getz and Shmuel, 2017). Experimentally, Ziser and Shmuel (2017) showed the tunability by voltage of flexural waves in a dielectric elastomer film, where Jia et al. (2016) and Yu et al. (2017) realized tunable noise suppressors based on pre-stretched dielectric elastomers membranes. Accordingly, dielectric elastomers have the potential to serve as electrostatically tunable sound filters, vibration reducers, and waveguides. However, the main drawback observed in all these investigations is that the required voltage to achieve significant tunability is extremely high. Since the electromechanical response (Tian et al., 2012) and band diagram characteristics (Sigmund and Jensen, 2003; Yi and Youn, 2016) can be improved by changing the composite initial microstructure, a possible resolution is to seek optimized unit cells; this is the objective of this work.

* Corresponding author.
E-mail address: meshmuel@tx.technion.ac.il (G. Shmuel).
[1] Present address: Structural Engineering Department, University of California, San Diego, USA.

https://doi.org/10.1016/j.ijsolstr.2018.03.014
0020-7683/

Our approach is based on *topology optimization*—a numerical method that systematically searches for the material distribution optimizing designated objective functions (Bendsøe and Kikuchi, 1988). Topology optimization has been employed for various applications (Bendsøe and Sigmund, 2003), and specifically for optimal band gaps (Sigmund and Jensen, 2003; Halkjær et al., 2006; Gazonas et al., 2006; Hussein et al., 2007; Bilal and Hussein, 2011; Liu et al., 2014; 2016; Li et al., 2016; Xie et al., 2017; Lu et al., 2017). For a comprehensive review we refer the reader to the excellent survey by Yi and Youn (2016). Generally speaking, the idea is to discretize the unit cell, such that the material properties of each element are the design parameters. The optimization process consists of an iterative derivation of the band diagram associated with design parameters that are assigned by optimization techniques. Notwithstanding the vast literature on topology optimization of different band gaps, only recently Hedayatrasa et al. (2016) employed such approach for nonlinear elastic deformation dependent gaps; topology optimization of dielectric elastomers has yet to be explored.

Our case study concerns anti-plane waves propagating in the periodicity plane of a fiber composite made of incompressible dielectric elastomer phases, deformed by a bias electric field along the fibers (Shmuel, 2013). As discussed earlier, the resultant band diagram is tunable, owing to an interplay between the bias electric field, quasi-static deformation and superposed wave propagation. The key parameters for band gap maximization are the material property contrast as well as the fiber filling fraction and shape. In our study, we focus on these latter parameters and we employ the *genetic algorithm* approach (Holland, 1992) to find unit cells that optimize at prescribed electric fields the width of the gap, or its relative change with respect to the unactuated state. Indeed, as the sequel shows, these objectives are improved by the choice of topology optimization-based unit cells. While our method is applied to anti-plane waves in specific types of composite and pre-deformation, it is extendible to more general settings. Specifically, it applies for in-plane waves of general propagation direction, as long their amplitude is small; it applies for compressible composites, as long as the constitutive behavior of the phases is linear, as indeed follows from the linearization about the deformed configuration; it applies for three-dimensional composites, as long as the microstructure is periodic, and for pre-deformations than maintain a periodic microstructure.

The presentation of our study starts with a summary of nonlinear and linearized electroelasticity theory in Section 2. This theory was employed by Shmuel (2013) to determine the quasi-static deformation of a soft composite of arbitrary fibers in response to an axial electric field, and develop the equations governing superposed anti-plane waves; these are revisited in Section 3, to provide a self-contained report. Section 4 is dedicated to the topology optimization of the dielectric elastomer composite for the objectives described in the introduction. We develop a method based on a fast plane wave expansion (FPWE) approach to determine the band diagram, and the genetic algorithm optimization which utilizes this method. Optimization results are presented and compared with the performance of the naive choice of a unit cell with circular fiber in Section 5. Conclusions and summary are given in Section 6.

2. Nonlinear and linearized electroelasticity

The modern description of nonlinear electroelasticity is given in Dorfmann and Ogden (2005); McMeeking and Landis (2005); Suo et al. (2008) and Dorfmann and Ogden (2010). In this Section we provide only the equations employed in the sequel; the reader is referred to the above references for the complete formulation.

Consider a composite made up of two incompressible homogeneous dielectric phases m and f, and surrounded by vacuum. In its *reference* configuration, the body occupies the volume region $\Omega_0^{(m)} \cup \Omega_0^{(f)} = \Omega_0 \subset \mathbb{R}^3$, whose boundary is $\partial\Omega_0$. Here and in the sequel, superscript (p) indicates quantities at phase p. When subjected to electromechanical loadings, the body is deformed and occupies the volume $\Omega^{(m)} \cup \Omega^{(f)} = \Omega$ with boundary $\partial\Omega$. The quasi-static deformation of the body is described by the vector field $\boldsymbol{\chi}$, which maps material particles from the reference configuration $\mathbf{X} \in \Omega_0$ to their current configuration $\mathbf{x} \in \Omega$. The deformation gradient $\mathbf{F} = \nabla_{\mathbf{X}}\boldsymbol{\chi}$ is computed with respect to the reference coordinates $\mathbf{X}$. The determinant $J = \det\mathbf{F}$ is the volume ratio of an infinitesimal element in the deformed configuration, dv, and its counterpart in the reference configuration, dV. Accordingly, incompressibility implies that $J = 1$.

The electrical fields in the dielectric satisfy

$$\nabla \cdot \mathbf{d} = 0, \quad \nabla \times \mathbf{e} = \mathbf{0}; \tag{1}$$

here, $\mathbf{e}$ is the electric field and $\mathbf{d}$ is the electric displacement field, and $\nabla\cdot(\bullet)$ and $\nabla\times(\bullet)$ are the divergence and curl operators with respect to $\mathbf{x}$.

When mechanical body forces are neglected, the symmetric *total* stress $\boldsymbol{\sigma}$ satisfies

$$\nabla \cdot \boldsymbol{\sigma} = \mathbf{0}. \tag{2}$$

The corresponding jump conditions between the two phases m and f are

$$[\![\boldsymbol{\sigma}]\!]\mathbf{n} = \mathbf{0}, \quad [\![\mathbf{d}]\!] \cdot \mathbf{n} = 0, \quad [\![\mathbf{e}]\!] \times \mathbf{n} = \mathbf{0}, \tag{3}$$

where $\mathbf{n}$ is the unit normal vector of a deformed area element, and $[\![\bullet]\!] = (\bullet)^{(m)} - (\bullet)^{(f)}$.

A formulation that uses $\mathbf{X}$ as the independent variable is based on the connections

$$\mathbf{P} = J\boldsymbol{\sigma}\mathbf{F}^{-\mathrm{T}}, \quad \mathbf{E} = \mathbf{F}^{\mathrm{T}}\mathbf{e}, \quad \mathbf{D} = J\mathbf{F}^{-1}\mathbf{d}. \tag{4}$$

The theory of Dorfmann and Ogden (2005) relates $\mathbf{P}$ and $\mathbf{E}$ to $\mathbf{F}$ and $\mathbf{D}$ via an *augmented* energy density function $\Psi(\mathbf{F}, \mathbf{D})$, as follows

$$\mathbf{P} = \frac{\partial\Psi}{\partial\mathbf{F}} - p_0\mathbf{F}^{-\mathrm{T}}, \qquad \mathbf{E} = \frac{\partial\Psi}{\partial\mathbf{D}}. \tag{5}$$

Here, p_0 is a *Lagrange multiplier* which accounts for the constraint of incompressibility.

Small-amplitude waves propagating in the deformed body are described in terms of the increments $\dot{\boldsymbol{\chi}}(\mathbf{X}, t)$ and $\dot{\mathbf{D}}(\mathbf{X}, t)$. The incremental equations are compactly written in terms of the connections

$$\boldsymbol{\Sigma} = \frac{1}{J}\dot{\mathbf{P}}\mathbf{F}^{\mathrm{T}}, \quad \check{\mathbf{e}} = \mathbf{F}^{-\mathrm{T}}\dot{\mathbf{E}}, \quad \check{\mathbf{d}} = \frac{1}{J}\mathbf{F}\dot{\mathbf{D}}, \tag{6}$$

namely,

$$\nabla \cdot \check{\mathbf{d}} = 0, \quad \nabla \times \check{\mathbf{e}} = \mathbf{0}, \quad \nabla \cdot \boldsymbol{\Sigma} = \rho\ddot{\mathbf{x}}, \tag{7}$$

where $\dot{\mathbf{x}}(\mathbf{x}, t) := \dot{\boldsymbol{\chi}}(\mathbf{X}, t)$. The field variables are related via the equations

$$\boldsymbol{\Sigma} = \mathscr{C}\mathbf{h} + p\mathbf{h} - \dot{p}\mathbf{I} + \mathscr{B}\check{\mathbf{d}}, \tag{8}$$

$$\check{\mathbf{e}} = \mathscr{B}^{\mathrm{T}}\mathbf{h} + \mathscr{A}\check{\mathbf{d}}. \tag{9}$$

Here, the increment in p is $\dot{p}$, the constitutive tensors $\mathscr{A}$, $\mathscr{B}$ and $\mathscr{C}$ are

$$\mathscr{A}_{ij} = JF^{-1}_{\alpha i}\frac{\partial^2\Psi}{\partial D_\alpha \partial D_\beta}F^{-1}_{\beta j}, \quad \mathscr{B}_{ijk} = F_{j\alpha}\frac{\partial^2\Psi}{\partial F_{i\alpha}\partial D_\beta}F^{-1}_{\beta k},$$
$$\mathscr{C}_{ijkl} = \frac{1}{J}F_{j\alpha}\frac{\partial^2\Psi}{\partial F_{i\alpha}\partial F_{k\beta}}F_{l\beta}, \tag{10}$$

and the displacement gradient $\mathbf{h} = \nabla\dot{\mathbf{x}}$ is subjected to the incompressibility constraint $\mathrm{tr}\mathbf{h} = 0$.

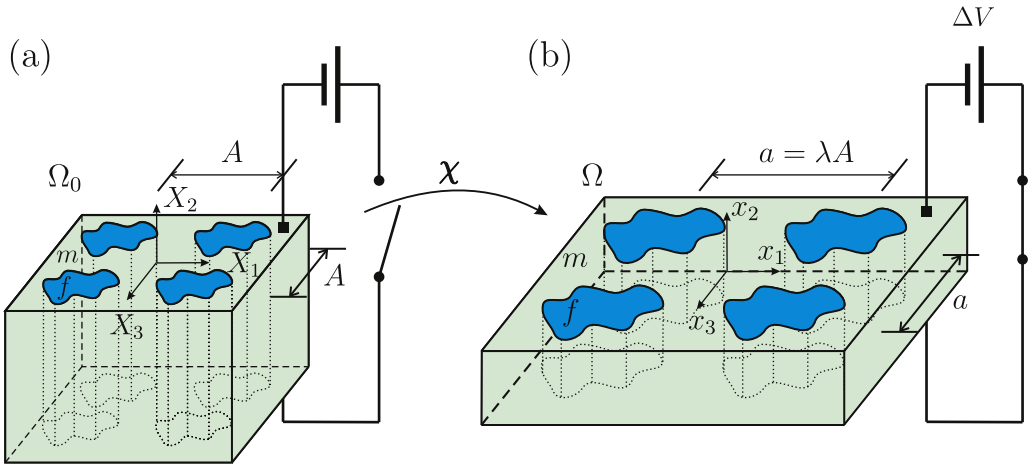

Fig. 1. Dielectric elastomer fiber composite in the (a) reference configuration, and (b) deformed configuration, when subjected to an axial electric field.

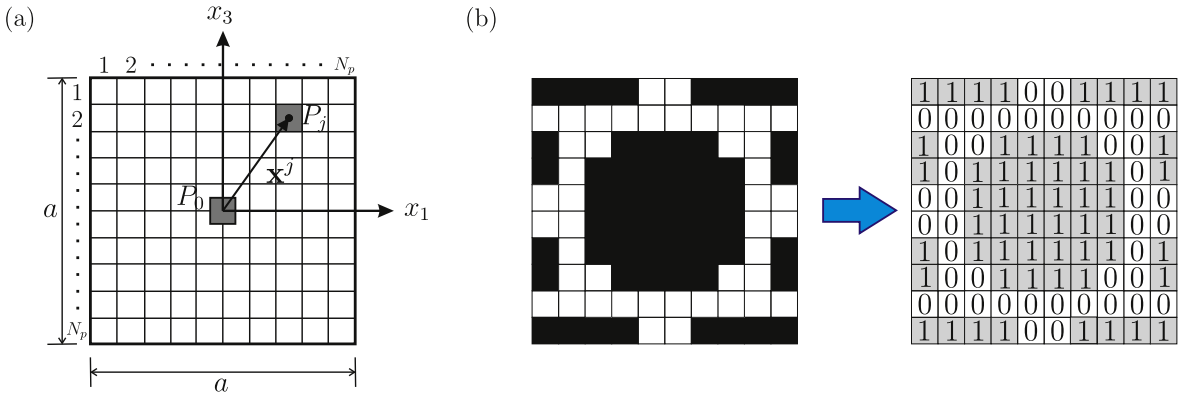

Fig. 2. (a) An $N_P \times N_P$ pixelized unit cell in the periodicity plane (x_1, x_3). On the basis of each fiber pixel $P_j \in \{P^{(f)}\}$ spatial coordinate $\mathbf{x}^j$, its characteristics are calculated from those of a central square fiber P_0 with the same dimensions. (b) Discretization of the unit cell into a bit-matrix of zeros and ones indicating matrix- and fiber-filled pixels, according to exemplary material distribution $\delta(\mathbf{x})$.

3. Nonlinear voltage-induced deformations and anti-plane waves in fiber composites

Band diagrams of dielectric elastomer composites are tunable by voltage-controlled nonlinear deformations. Owing to the bias electric field and resultant strains, the physical and geometrical properties of the phases change; in turn, the propagation of superposed elastic waves changes too. Since the voltage-deformation relation of the phases is highly nonlinear, different magnitudes of voltage result in significantly different deformations and instantaneous moduli, and in turn, significantly different band structures. This approach to achieve tunability has been demonstrated in a series of works (Shmuel and deBotton, 2012; Shmuel, 2013; Getz et al., 2017; Getz and Shmuel, 2017). For completeness, we summarize next the case studied in Shmuel (2013) of anti-plane waves in a fiber composite, which was deformed by an axial electric field. Later on, we will apply topology optimization schemes to find unit cell geometries that optimize prescribed gap characteristics, upon the composite actuation.

Consider an infinite dielectric elastomer composite, which is periodic in the (x_1, x_3) plane. The composite periodic cell is made up of a fiber of arbitrary cross section (phase f), in a different matrix (phase m). Repetitions of the unit cell are arranged in a square lattice with periodicity A, *see* Fig. 1(a). The composite is subjected to an average electric field $e_2\mathbf{i}_2$,[2] where $\mathbf{i}_j$ is a unit vector in the x_j direction, see Fig. 1(b).

The resultant deformation depends on the constitutive behavior of the phases constituting the composite, which we assume described by the *augmented* Gentian functions

$$\Psi^{(p)}(\mathbf{F}, \mathbf{D}) = -\frac{\mu^{(p)} J_m^{(p)}}{2} \ln\left[1 - \frac{\mathrm{tr}(\mathbf{F}^{\mathrm{T}}\mathbf{F}) - 3}{J_m^{(p)}}\right] + \frac{1}{2\epsilon^{(p)}} \mathbf{D} \cdot \mathbf{F}^{\mathrm{T}}\mathbf{F}\mathbf{D}; \tag{11}$$

here, $\mu^{(p)}$ is the shear modulus, $\epsilon^{(p)}$ is the dielectric constant, and $J_m^{(p)}$ models the strain stiffening exhibited by elastomers.

When the phases are perfectly bonded and the only load is the prescribed electric field, Shmuel (2013) found that the deformation and the electric field are homogeneous in the form

$$\mathsf{F}^{(m)} = \mathsf{F}^{(f)} = \mathrm{diag}\left[\lambda, \lambda^{-2}, \lambda\right], \qquad \mathbf{e}^{(m)} = \mathbf{e}^{(f)} = e\mathbf{i}_2, \tag{12}$$

and are related via

$$\breve{\bar{\mu}}\left(\lambda^2 - \lambda^{-4}\right) = \bar{\epsilon} e^2, \tag{13}$$

where $\breve{\mu}^{(p)} = \frac{\mu^{(p)}}{1-(2\lambda^2+\lambda^{-4}-3)/J_m^{(p)}}$, $\bar{(\bullet)} = v^{(m)}(\bullet) + v^{(f)}(\bullet)$ and $v^{(p)}$ is the volume fraction of phase p. To arrive at this result, Shmuel (2013) postulated a deformation from the outset, and verified it

[2] This is achieved by applying voltage to electrodes coating the composite at the far surfaces.

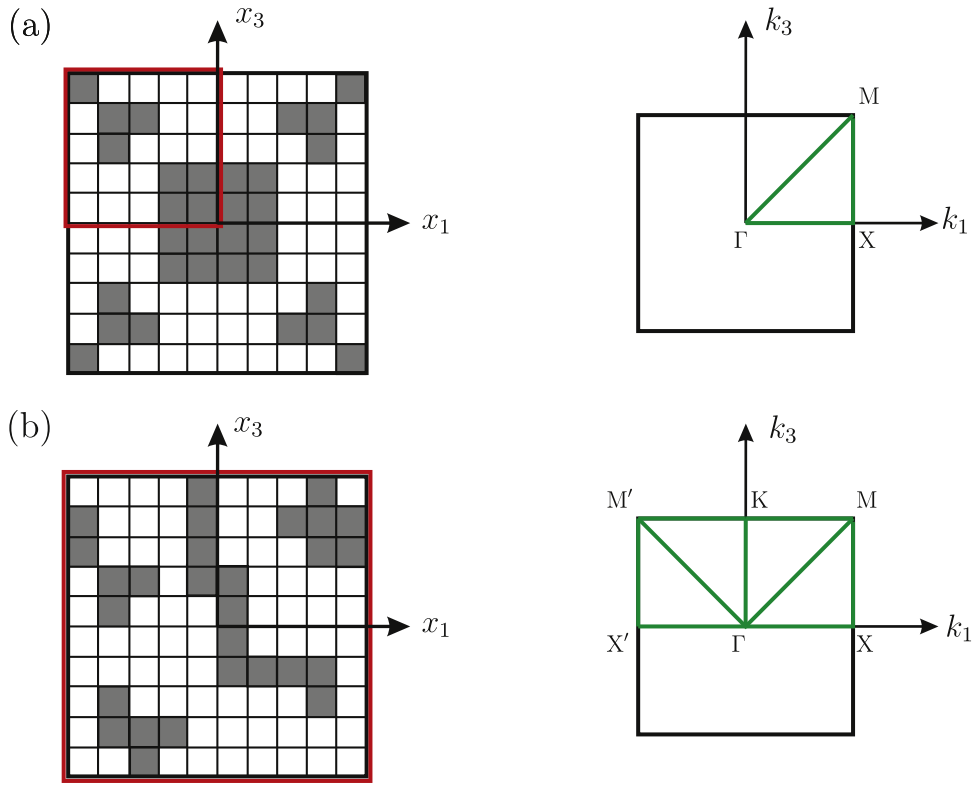

Fig. 3. Exemplary unit cells (left panels) and corresponding scanned segments in the Brillouin zones to determine the gaps extrema (indicated in green in the right panels) for (a) the symmetric and (b) asymmetric cases. The domain, on which material distribution is optimized, is indicated by a red contour. (For interpretation of the references to colour in this figure legend, the reader is referred to the web version of this article.)

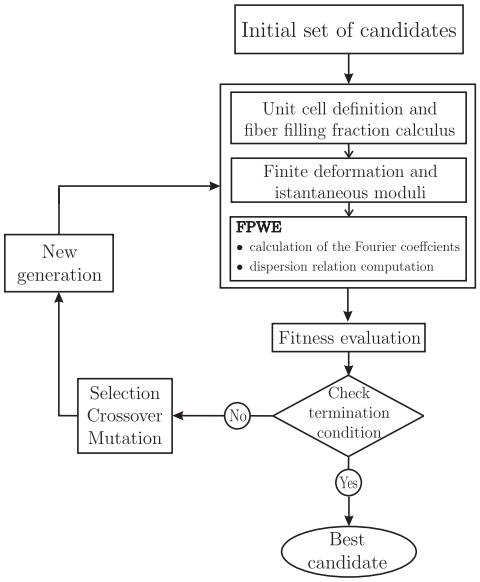

Fig. 4. A schematic representation of the optimization procedure.

can satisfy the balance laws and boundary conditions. The resultant equations delivered relation (13).

We are concerned with anti-plane waves propagating in the (x_1, x_3) plane of the deformed composite. The equations for the corresponding electric and elastic displacement fields are

$$\Sigma_{21,1}(\mathbf{x},t)+\Sigma_{23,3}(\mathbf{x},t)=\rho(\mathbf{x})\dot{x}_{2,tt}, \tag{14}$$

$$\check{d}_{1,1}(\mathbf{x},t)+\check{d}_{3,3}(\mathbf{x},t)=0. \tag{15}$$

Making use of the linearized constitutive relations, Eqs. (14) and (15) obtain the form

$$\nabla_{\mathrm{T}}\cdot(\tilde{\mu}(\mathbf{x})\nabla_{\mathrm{T}}\dot{x}_2(\mathbf{x},t)-d_2(\mathbf{x})\nabla_{\mathrm{T}}\varphi(\mathbf{x},t))=\rho(\mathbf{x})\dot{x}_{2,tt}, \tag{16}$$

$$\nabla_{\mathrm{T}}\cdot(-d_2(\mathbf{x})\nabla_{\mathrm{T}}\dot{x}_2(\mathbf{x},t)-\epsilon(\mathbf{x})\nabla_{\mathrm{T}}\varphi(\mathbf{x},t))=0. \tag{17}$$

Here, $\varphi(x_1, x_3, t)$ is a scalar potential from which $\check{\mathbf{e}}$ is calculated such that $\check{\mathbf{e}}=-\nabla\varphi$, $\tilde{\mu}(\mathbf{x})=\check{\mu}(\mathbf{x})\lambda^2-\epsilon(\mathbf{x})e_2^2$, and $\nabla_{\mathrm{T}}(\bullet)=(\bullet)_{,1}\mathbf{i}_1+(\bullet)_{,3}\mathbf{i}_3$ is the in-plane gradient operator. Eqs. (14)–(17), which govern the band diagram, do not admit an analytic solution. A method to obtain numerical solutions is described next. We clarify that while in the analysis to follow it is sufficient to analyze single and finite unit-cell (in virtue of Bloch theorem), the composite we are analyzing is infinite. As such, Eqs. (16)–(17) are not subjected to external boundary conditions, and our objective is to understand what kind of how elastic waves may propagate (or not), before addressing specific conditions other than the equations of motion and Maxwell equations.

4. Fast plane wave expansion method and genetic algorithm

Our goal is to determine the fiber distribution in the unit cell that optimizes desired band gap characteristics. To this end, in this section we first introduce the FPWE method for calculating the band diagram (Liu et al., 2014; Xie et al., 2017). Subsequently, we present an optimization procedure based on the genetic algorithm (Holland, 1992). We note that for the applicability of the FPWE method, the medium should be periodic, and the amplitude of the waves should be small. Additionally, the constitutive behavior of the phases should be linear, as indeed follows from the linearization about the deformed configuration.

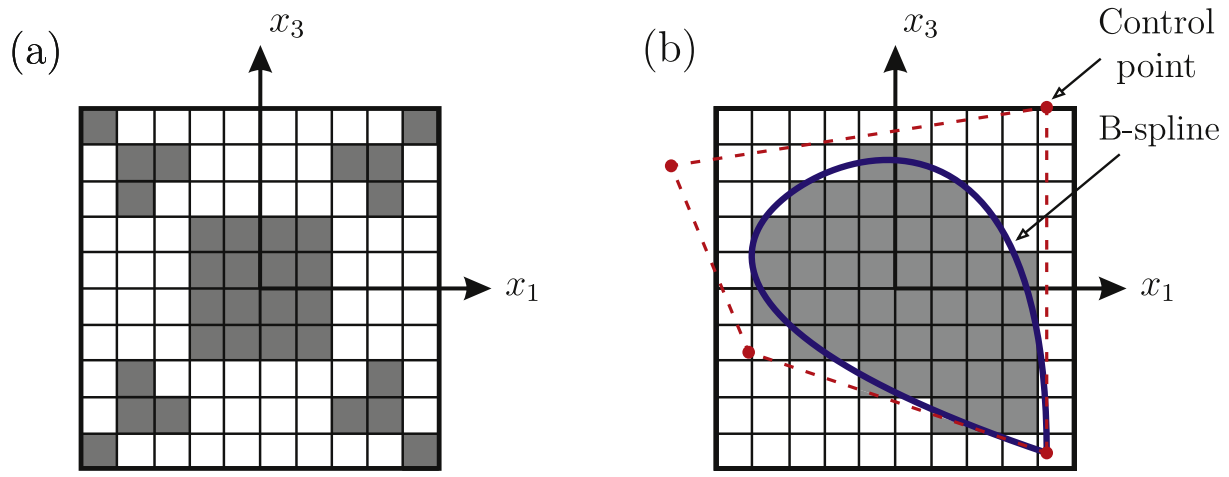

Fig. 5. (a) Pixel grid-based and (b) closed B-spline projection-based representations of the unit cell.

4.1. Fast plane wave expansion method

The method starts with partitioning the unit cell into $N_\mathrm{P} \times N_\mathrm{P}$ pixels, see Fig. 2(a). Each pixel corresponds either to the matrix phase m or the fiber phase f. Thus, the design of the composite structure is determined by the choice of the material in each pixel.

The material distribution in the unit cell is described using a characteristic function of the pixel center position $\mathbf{x}^j$, defined as

$$\delta\left(\mathbf{x}^j\right) = \begin{cases} 1 & \mathbf{x}^j \subset \Omega^{(f)}, \\ 0 & \mathbf{x}^j \not\subset \Omega^{(f)}, \end{cases} \tag{18}$$

where $j = 1, \ldots, N_\mathrm{P}^2$. Accordingly, the unit cell is represented by a bit-string of zeros and ones indicating matrix- and fiber-filled pixels, $\mathrm{M}^\delta = \left[\delta\left(\mathbf{x}^1\right), \ldots, \delta\left(\mathbf{x}^{N_\mathrm{P}^2}\right)\right]$, as in Fig. 2(b).

We recall that the material parameters are periodic functions of x_1 and x_3. The FPWE method exploits this to represent material properties in Fourier series such that

$$\zeta\left(\mathbf{x}\right) = \sum_{\mathbf{G}} \zeta\left(\mathbf{G}\right) \exp\left(\mathrm{i}\mathbf{G}\cdot\mathbf{x}\right), \qquad \zeta = \hat{\mu}, \rho. \tag{19}$$

Here, $\{\mathbf{G}\}$ is the infinite set of reciprocal lattice vectors. Since the Bravais lattice of the composite in the deformed state is based on a square unit cell of period $a = \lambda A$, the reciprocal lattice is $\left\{\mathbf{G} = \frac{2\pi}{a} n_1 \mathbf{i}_1 + \frac{2\pi}{a} n_3 \mathbf{i}_3,\ n_1, n_3 \in \mathbb{N}\right\}$. The set of Fourier coefficients $\{\zeta(\mathbf{G})\}$ associated with the reciprocal lattice vectors $\{\mathbf{G}\}$ is defined by

$$\zeta\left(\mathbf{G}\right) = \frac{1}{a^2} \iint_{s_\mathrm{cell}} \zeta\left(\mathbf{x}\right) \exp\left(-\mathrm{i}\mathbf{G}\cdot\mathbf{x}\right)\mathrm{d}s, \tag{20}$$

where s_cell is the area of the unit cell in Ω.

Taking advantage of the fact that $\zeta(\mathbf{x})$ is piecewise constant at $\mathbf{x} \in \Omega^{(m)}$ and $\mathbf{x} \in \Omega^{(f)}$, we can write the Fourier coefficients of a square fiber P_0, with the same side length of the pixels a/N_P, placed at the center of the unit cell as

$$\zeta_0(\mathbf{G}) = \begin{cases} v_\mathrm{P}\zeta^{(f)} + (1 - v_\mathrm{P})\zeta^{(m)} & \mathbf{G} = \mathbf{0}, \\ \left(\zeta^{(f)} - \zeta^{(m)}\right) F(\mathbf{G}) & \mathbf{G} \neq \mathbf{0}, \end{cases} \tag{21}$$

where

$$F(\mathbf{G}) = \frac{1}{a^2} \iint_{s_\mathrm{P}} \exp\left(-\mathrm{i}\mathbf{G}\cdot\mathbf{x}\right)\mathrm{d}s = v_\mathrm{P}\mathrm{sinc}\left(\frac{G_1 a}{2N_\mathrm{P}}\right)\mathrm{sinc}\left(\frac{G_3 a}{2N_\mathrm{P}}\right); \tag{22}$$

here $v_\mathrm{P} = 1/N_\mathrm{P}^2$ and s_P are the volume fraction and area of the square fiber P_0 in Ω, respectively. The Fourier coefficients of any fiber pixel $P_j \in \{P^{(f)}\}$ in the unit cell are calculated from those of the central square fiber P_0, according to the pixel location with respect to the center of the unit cell $\mathbf{x}^j$ and the characteristic function $\delta(\mathbf{x}^j)$. The Fourier coefficients of the whole unit cell are accordingly

$$\zeta\left(\mathbf{G}\right) = \begin{cases} n_\mathrm{Pf} v_\mathrm{P} \zeta + (1 - n_\mathrm{Pf} v_\mathrm{P})\zeta^{(m)} & \mathbf{G} = \mathbf{0}, \\ \left(\zeta^{(f)} - \zeta^{(m)}\right) F(\mathbf{G}) g(\mathbf{G}) & \mathbf{G} \neq \mathbf{0}. \end{cases} \tag{23}$$

Here, n_Pf is the total number of fiber pixels in the unit cell and $g(\mathbf{G})$ is given by

$$g(\mathbf{G}) = \sum_{j=1}^{N_\mathrm{P}^2} \exp\left(\mathrm{i}\mathbf{G}\cdot\mathbf{x}^j\right)\delta\left(\mathbf{x}^j\right). \tag{24}$$

As established by the Bloch theorem (Kittel, 2005), the incremental fields $\dot{x}_2$ and φ are expressible in the form

$$\xi\left(\mathbf{x}, t\right) = \sum_{\mathbf{G}} \xi\left(\mathbf{G}\right) \exp\left[\mathrm{i}(\mathbf{G}+\mathbf{k})\cdot\mathbf{x} - \mathrm{i}\omega t\right], \qquad \xi = \dot{x}_2, \varphi, \tag{25}$$

where the Bloch wave vector is $\mathbf{k} = k_1\mathbf{i}_1 + k_3\mathbf{i}_3$, $k_1, k_3 \in \mathbb{R}$, and ω is the angular frequency. Utilizing Eqs. (21) and (25), we write Eqs. (16) and (17) as follows

$$\begin{aligned} &\Big\{ \sum_{\mathbf{G},\mathbf{G}'} \Big[\left(\tilde{\mu}\left(\mathbf{G}\right)\dot{x}_2\left(\mathbf{G}'\right) - d_2\left(\mathbf{G}\right)\varphi\left(\mathbf{G}'\right)\right)\left(\mathbf{G}'+\mathbf{k}\right)\cdot\left(\mathbf{G}+\mathbf{G}'+\mathbf{k}\right) \\ &\quad -\omega^2\rho\left(\mathbf{G}\right)\dot{x}_2\left(\mathbf{G}'\right)\Big] \\ &\quad \exp\left[\mathrm{i}\left(\mathbf{G}+\mathbf{G}'\right)\cdot\mathbf{x} - \mathrm{i}\omega t\right]\Big\} \exp\left(\mathrm{i}\mathbf{k}\cdot\mathbf{x}\right) = 0, \end{aligned} \tag{26}$$

$$\begin{aligned} &\Big\{ \textstyle\sum_{\mathbf{G},\mathbf{G}'} \left[\left(-d_2\left(\mathbf{G}\right)\dot{x}_2\left(\mathbf{G}'\right) - \epsilon\left(\mathbf{G}\right)\varphi\left(\mathbf{G}'\right)\right)\left(\mathbf{G}'+\mathbf{k}\right)\cdot\left(\mathbf{G}+\mathbf{G}'+\mathbf{k}\right)\right] \\ &\quad \exp\left[\mathrm{i}\left(\mathbf{G}+\mathbf{G}'\right)\cdot\mathbf{x} - \mathrm{i}\omega t\right]\Big\} \exp\left(\mathrm{i}\mathbf{k}\cdot\mathbf{x}\right) = 0. \end{aligned} \tag{27}$$

Eqs. (26) and (27) hold for any $\mathbf{x}$, and it follows the sums in the curly brackets vanish. We multiply these sums by $\exp\left(-i\mathbf{G}''\cdot\mathbf{x}\right)$, and integrate the result over the unit-cell; since the only non-vanishing terms are those satisfying the condition $\mathbf{G}'' = \mathbf{G} + \mathbf{G}'$, the resultant equations are

$$\begin{aligned} &\sum_{\mathbf{G}'} \left(\tilde{\mu}\left(\mathbf{G}-\mathbf{G}'\right)\dot{x}_2\left(\mathbf{G}'\right) - d_2\left(\mathbf{G}-\mathbf{G}'\right)\varphi\left(\mathbf{G}'\right)\right)\left(\mathbf{G}'+\mathbf{k}\right)\cdot\left(\mathbf{G}+\mathbf{k}\right) \\ &\quad = \omega^2 \sum_{\mathbf{G}'} \rho\left(\mathbf{G}-\mathbf{G}'\right)\dot{x}_2\left(\mathbf{G}'\right), \end{aligned} \tag{28}$$

$$\sum_{\mathbf{G}'} \left(-d_2\left(\mathbf{G}-\mathbf{G}'\right)\dot{x}_2\left(\mathbf{G}'\right) - \epsilon\left(\mathbf{G}-\mathbf{G}'\right)\varphi\left(\mathbf{G}'\right)\right)\left(\mathbf{G}'+\mathbf{k}\right)\cdot\left(\mathbf{G}+\mathbf{k}\right) = 0. \tag{29}$$

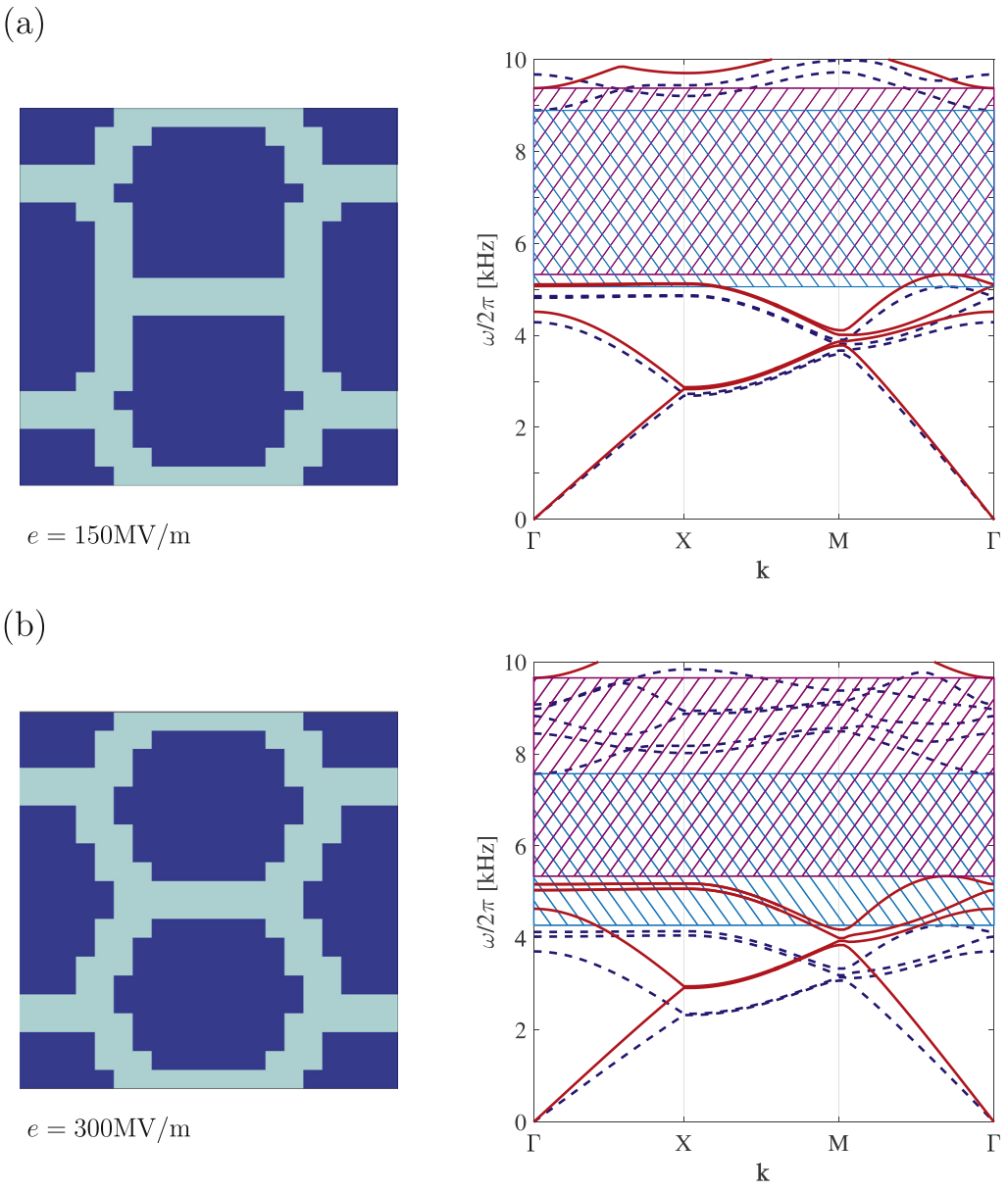

Fig. 6. Symmetric unit cells optimizing the gap width (left panels) at (a) $e = 150$ MV/m and (b) $e = 300$ MV/m, obtained using the pixel grid representation. Corresponding band diagrams are depicted in the right panels. Specifically, the eigenfrequencies in the reference and in the actuated configuration are shown by continuous red and dashed blue curves, respectively, as functions of $\mathbf{k}$ along the edges of the Brillouin zone. Left- and right-hatched areas indicate the band gaps in the actuated and in the reference states, respectively. (For interpretation of the references to colour in this figure legend, the reader is referred to the web version of this article.)

Eqs. (28) and (29) admit the matrix form

$$\begin{bmatrix} \mathsf{Q}^{(1,1)} & \mathsf{Q}^{(1,2)} \\ \mathsf{Q}^{(2,1)} & \mathsf{Q}^{(2,2)} \end{bmatrix} \begin{Bmatrix} \dot{\mathsf{x}}_2(\mathbf{G}') \\ \varphi(\mathbf{G}') \end{Bmatrix} = \omega^2 \begin{bmatrix} \mathsf{R}^{(1,1)} & 0 \\ 0 & 0 \end{bmatrix} \begin{Bmatrix} \dot{\mathsf{x}}_2(\mathbf{G}') \\ \varphi(\mathbf{G}') \end{Bmatrix}, \tag{30}$$

where $\dot{\mathsf{x}}_2$ and $\varphi(\mathbf{G}')$ are column vectors of the components $\dot{x}_2(\mathbf{G}')$ and $\varphi(\mathbf{G}')$, and the components of the matrices $\mathsf{Q}^{(1,1)}$, $\mathsf{Q}^{(1,2)}$, $\mathsf{Q}^{(2,1)}$, $\mathsf{Q}^{(2,2)}$ and $\mathsf{R}^{(1,1)}$ are

$$\mathsf{Q}^{(1,1)}_{\mathbf{G},\mathbf{G}'} = \tilde{\mu}(\mathbf{G}-\mathbf{G}')(\mathbf{G}'+\mathbf{k})\cdot(\mathbf{G}+\mathbf{k}), \tag{31}$$

$$\mathsf{Q}^{(1,2)}_{\mathbf{G},\mathbf{G}'} = -d_2(\mathbf{G}-\mathbf{G}')(\mathbf{G}'+\mathbf{k})\cdot(\mathbf{G}+\mathbf{k}), \tag{32}$$

$$\mathsf{Q}^{(1,2)}_{\mathbf{G},\mathbf{G}'} = \mathsf{Q}^{(2,1)}_{\mathbf{G},\mathbf{G}'}, \tag{33}$$

$$\mathsf{Q}^{(1,1)}_{\mathbf{G},\mathbf{G}'} = -\epsilon(\mathbf{G}-\mathbf{G}')(\mathbf{G}'+\mathbf{k})\cdot(\mathbf{G}+\mathbf{k}), \tag{34}$$

$$\mathsf{R}^{(1,1)}_{\mathbf{G},\mathbf{G}'} = \rho(\mathbf{G}-\mathbf{G}'). \tag{35}$$

Substituting the relation $\varphi(\mathbf{G}') = -\left(\mathsf{Q}^{(2,2)}\right)^{-1}\mathsf{Q}^{(2,1)}\dot{\mathsf{x}}_2(\mathbf{G}')$, we finally obtain

$$\mathsf{M}\dot{\mathsf{x}}_2 = \omega^2 \mathsf{R}\dot{\mathsf{x}}_2, \tag{36}$$

where $\mathsf{M} = \mathsf{Q}^{(1,1)} - \mathsf{Q}^{(1,2)}\left(\mathsf{Q}^{(2,2)}\right)^{-1}\mathsf{Q}^{(2,1)}$.

The band diagram is computed by solving a finite version of Eq. (36) for ω as a function of $\mathbf{k}$ for a chosen finite subset of $\{\mathbf{G}\}$.

Under certain conditions, to calculate the gaps it is sufficient to consider only wave vectors at edges of the Brillouin zone (Craster et al., 2012). If the unit cell is symmetric with respect to x_1 and x_3 directions, these edges are between the points $\Gamma = (0,0)$, $\mathrm{X} = (\pi/a, 0)$ and $\mathrm{M} = (\pi/a, \pi/a)$, illustrated by the green segments in the right panel of Fig. 3(a). If the unit cell is not symmetric additional edges between the points Γ, M and $\mathrm{K} = (0, \pi/a)$ are needed

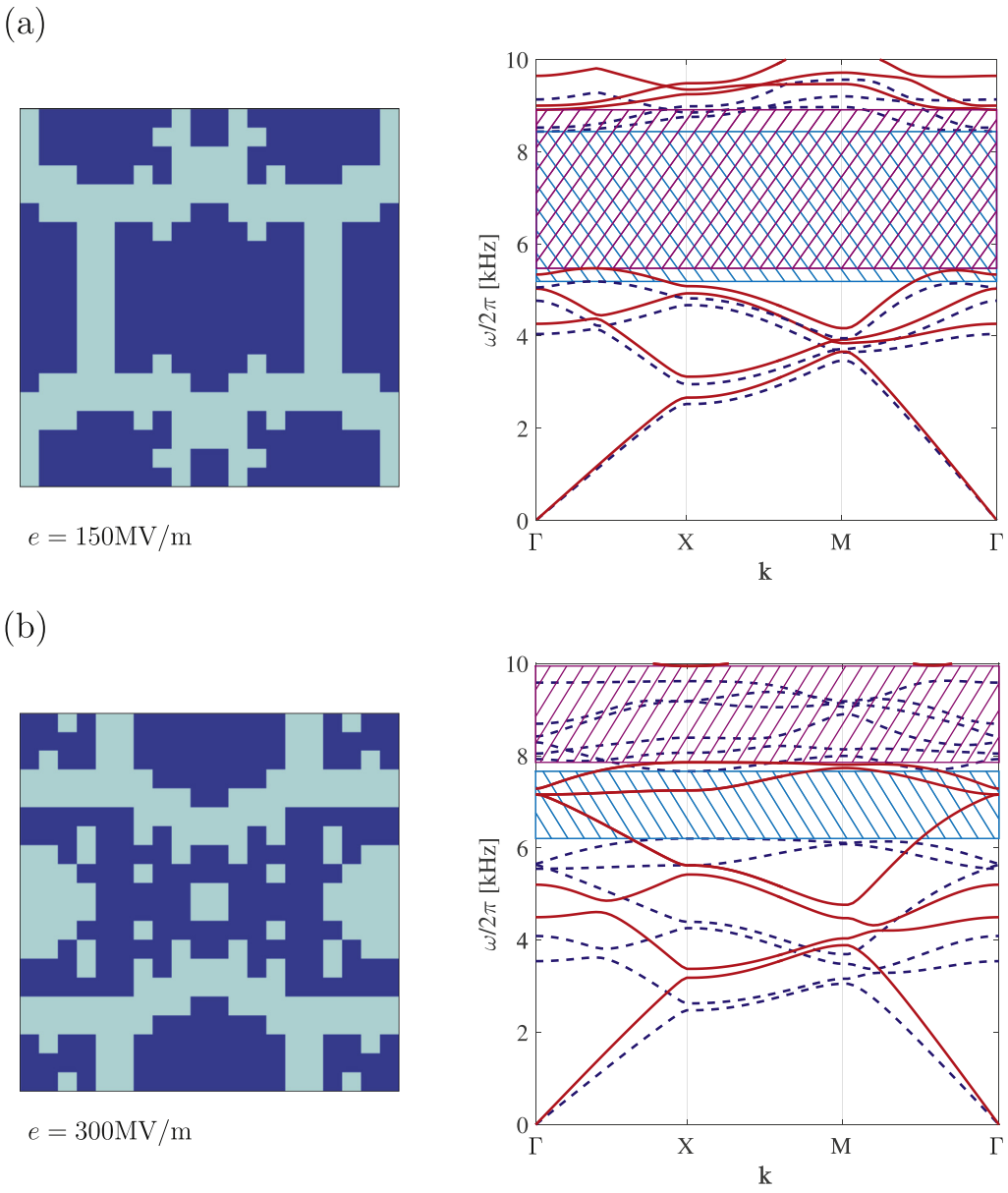

Fig. 7. Symmetric unit cells optimizing the relative change in the gap width (left panels) at (a) $e = 150$ MV/m and (b) $e = 300$ MV/m, obtained using the pixel grid representation. Corresponding band diagrams are depicted in the right panels. Specifically, the eigenfrequencies in the reference and in the actuated configuration are shown by continuous red and dashed blue curves, respectively, as functions of **k** along the edges of the Brillouin zone. Left- and right-hatched areas indicate the band gaps in the actuated and in the reference states, respectively. (For interpretation of the references to colour in this figure legend, the reader is referred to the web version of this article.)

(Yi and Youn, 2016; Meng et al., 2017), illustrated by the green segments in the right panel in Fig. 3(b).

In our computations to follow, a number of 441 plane waves, corresponding to $-10 < n_1, n_3 < 10$ was found sufficient for the convergence of the band diagram. For further details on the method convergence, see the Appendix.

4.2. Genetic algorithm and optimization procedure

Our optimization is based on a genetic algorithm approach (Holland, 1992). The algorithm starts with a pool of unit cell candidates. Each candidate is represented by a vector of its design variables. For each candidate, our scheme calculates the finite deformation in response to a prescribed electric field, and the resultant band diagram using FPWE. We emphasize that the finite deformation and, in turn, the instantaneous moduli, depend on the fiber filling fraction of each candidate. Therefore, the material properties that are used in the FPWE differ between candidates of different filling fraction. According to a certain objective or *fitness* function, the genetic algorithm rates the band diagram of each candidate. Then, in order to create a new generation of candidates with higher fitness values, the algorithm applies the following operators. *Selection* elects, on the basis of the fitness value, a portion of the existing pool of candidates to create a new generation via *crossover*—an exchange of a section of the variable vectors of two candidates. *Mutation* corresponds to a random modification of the variable vector of a candidate. The procedure is iterated until the average change in the best fitness value over a certain number of generations is less than or equal to a selected tolerance. A schematic representation of the optimization procedure is depicted in Fig. 4.

To represent the unit cell, we employ two different approaches. The first approach is based on a representation of the unit cell by means of the pixel grid only, as depicted in Fig. 5(a). Thereby, the

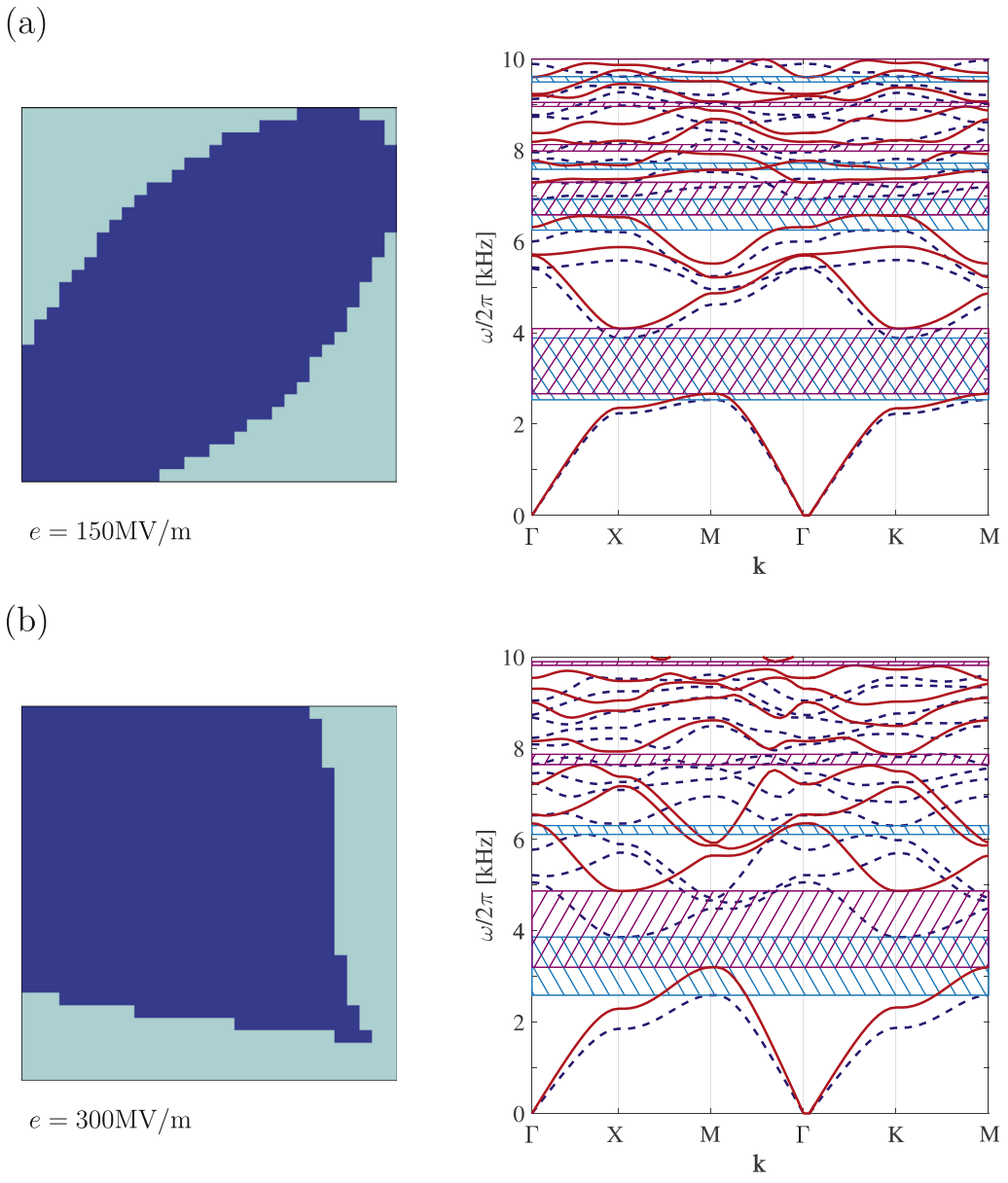

Fig. 8. Unit cells optimizing the gap width (left panels) at (a) $e = 150$ MV/m and (b) $e = 300$ MV/m, obtained using the four points B-spline representation. Corresponding band diagrams are depicted in the right panels. Specifically, the eigenfrequencies in the reference and in the actuated configuration are shown by continuous red and dashed blue curves, respectively, as functions of **k** along the edges of the Brillouin zone. Left- and right-hatched areas indicate the band gaps in the actuated and in the reference states, respectively. (For interpretation of the references to colour in this figure legend, the reader is referred to the web version of this article.)

fiber inclusion is represented by the filled pixels. The design variables of the unit cell are given by the components of the material distribution bit-string M^{δ} and their number is hence N_{p}^2. Clearly, as N_{p} increases, the searching space for the optimal solution increases exponentially, since the number of possible unit cells is $2^{\frac{N_{\mathrm{p}}}{4}\left(\frac{N_{\mathrm{p}}}{2}+1\right)}$. If symmetry of the unit cell with respect to x_1 and x_3 direction is assumed, for example as in Fig. 3(a), the number of design variables is reduced to $N_{\mathrm{p}}^2/4$. In this approach, each pixel is assigned with fiber or matrix properties independently of its neighbors, such that the creation of multiple fiber inclusions is straightforward.

Alternatively, the fiber can be represented via a closed B-spline as shown in Fig. 5(b) (Vondřejc et al., 2017). The B-spline is identified by the coordinates of its control points, whose number depends on the B-spline order. The closed B-spline then is mapped onto a pixel grid identifying fiber and matrix pixels. Fiber properties will be assigned to pixels whose center lies within the space identified by the closed B-spline. The design variables in this case are given by the coordinates of the B-spline control points. The number of variables in the optimization problem is significantly lower than the pixel gird representation. In the present formulation, this approach, being based on a single B-spline, allows for the representation of only one inclusion in the unit cell. This drawback can be overcome by considering multiple B-splines representing separate inclusions, that are optimized simultaneously. In the implementation to follow, we restrict attention to the single B-spline formulation, and thus, we obtain only a single inclusion in this representation.

In our case study, we focus on the sonic band gap across the audible frequency range 0–10 kHz. The optimization is carried out with respect to (i) the gap width in the actuated configuration, or (ii) the relative change in the gap width owing to the electric actuation. The fitness function we seek to maximize for the first ob-

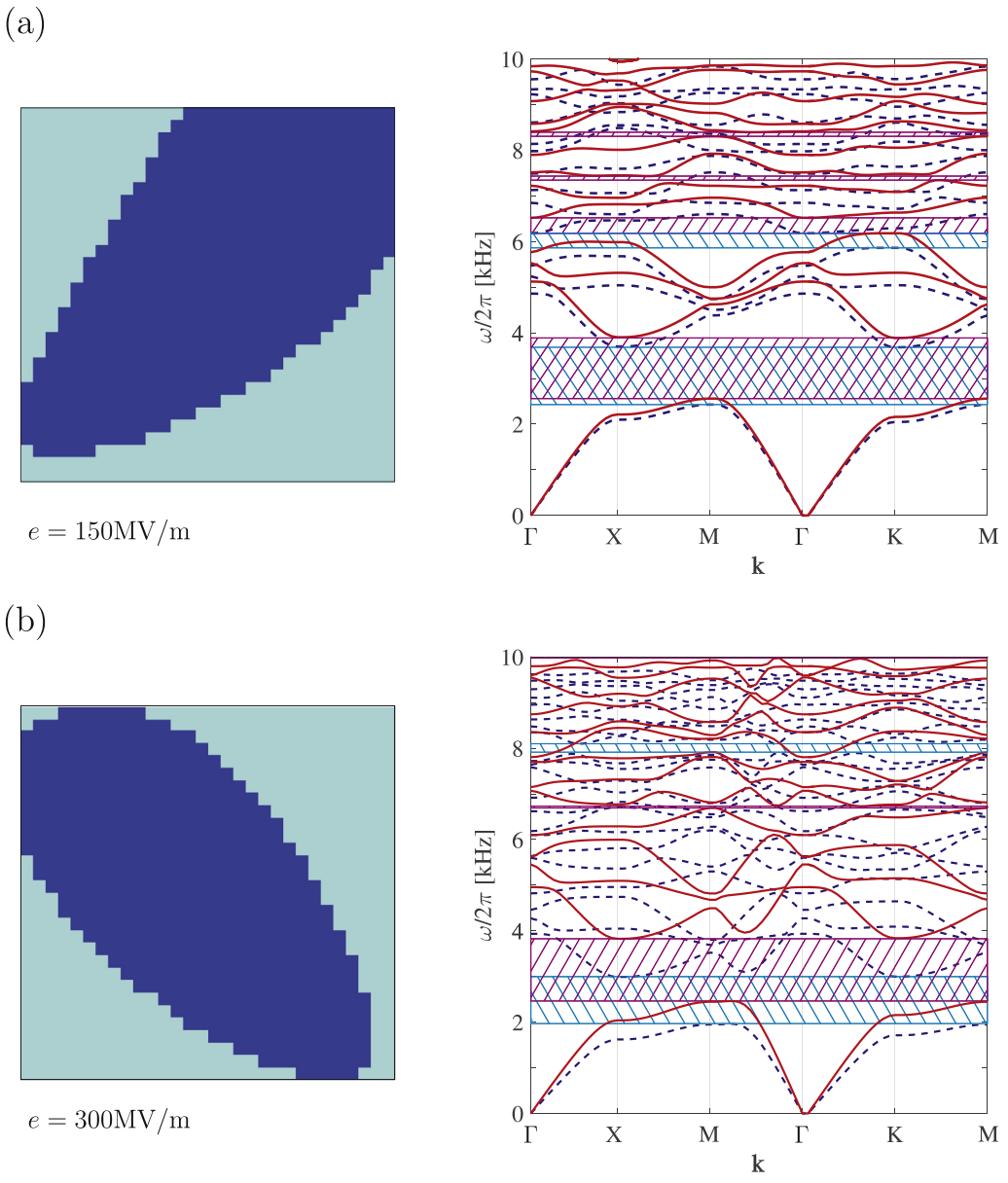

Fig. 9. Unit cells optimizing the relative change in the gap width (left panels) at (a) $e = 150$ MV/m and (b) $e = 300$ MV/m, obtained using the four points B-spline representation. Corresponding band diagrams are depicted in the right panels. Specifically, the eigenfrequencies in the reference and in the actuated configuration are shown by continuous red and dashed blue curves, respectively, as functions of $\mathbf{k}$ along the edges of the Brillouin zone. Left- and right-hatched areas indicate the band gaps in the actuated and in the reference states, respectively. (For interpretation of the references to colour in this figure legend, the reader is referred to the web version of this article.)

jective is

$$f_{BG}(\mathbf{Y}) = \begin{cases} 10\text{kHz} - \max_{\mathbf{k}} \left(\omega_n(\mathbf{Y}, \mathbf{k})\right) \\ \quad \text{if } \min_{\mathbf{k}} \left(\omega_{n+1}(\mathbf{Y}, \mathbf{k})\right) \geq 10\text{kHz}, \\ \min_{\mathbf{k}} \left(\omega_{n+1}(\mathbf{Y}, \mathbf{k})\right) - \max_{\mathbf{k}} \left(\omega_n(\mathbf{Y}, \mathbf{k})\right) \\ \quad \text{if } \min_{\mathbf{k}} \left(\omega_{n+1}(\mathbf{Y}, \mathbf{k})\right) < 10\text{kHz}. \end{cases} \tag{37}$$

Here, $\min_{\mathbf{k}}(\omega_n(\mathbf{Y}, \mathbf{k}))$ and $\max_{\mathbf{k}}(\omega_n(\mathbf{Y}, \mathbf{k}))$ denote the minimum and maximum of the nth eigenfrequency ω_n over $\mathbf{k}$ for a given design of the unit cell, $\mathbf{Y}$, respectively.

The fitness function to maximize for the second objective is

$$f_T(\mathbf{Y}) = \frac{f_{BG}(\mathbf{Y}) - f^0_{BG}(\mathbf{Y})}{f^0_{BG}(\mathbf{Y})}. \tag{38}$$

Here, $f^0_{BG}(\mathbf{Y})$ is the gap width associated with the undeformed composite. Accordingly, its functional form is similar to $f_{BG}(\mathbf{Y})$, with the difference that the scanned Brillouin zone is bounded by $|k_i| \leq \pi/A$ and not π/a.

5. Topology optimization results

We present next the optimization results for the objective functions in Eqs. (37) and (38), through the two different methods of unit cell representation. In the first case, the unit cell is discretized into a 20×20 pixel grid, while in the latter case we employ a 30×30 pixel grid, as the number of design variables is independent of the number of pixels. The optimization procedure has been implemented in Matlab, using its built-in genetic algorithm.

For the material constants, we use the composite in modeled (Getz et al., 2017), namely, fibers made of polyurethane PT6100S by Deerfield embedded in a matrix made of silicone CF19-2186 by Nusil. The corresponding properties of these products are summarized in Table 1.

Table 1
The density ρ, shear modulus μ, relative permittivity ϵ_r, locking parameter J_m and dielectric strength of silicone CF19-2186 by Nusil and polyurethane PT6100S by Deerfield.

Material	ρ [kg/m^3]	μ [kPa]	ϵ_r	J_m	Dielectric strength [MV/m]
Silicone CF19-2186	1100	333	2.8	46.3	235
Polyurethane PT6100S	1200	5667	7	6.67	160

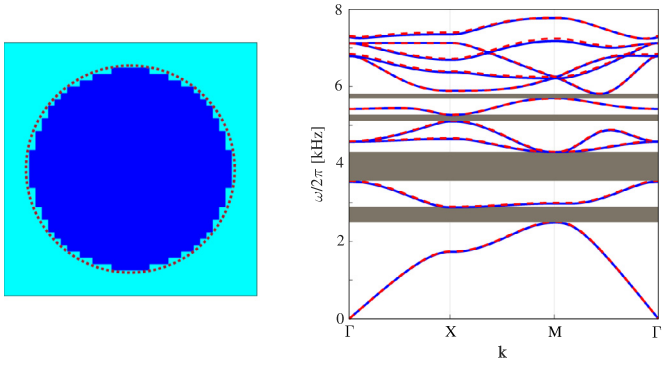

Fig. 10. A circular fiber and its pixelized approximation (left panel) analyzed by the PWE and the FPWE methods are, respectively, in the right panel. Eigenfrequencies obtained by employing the PWE and FPWE methods are shown by solid blue and dashed red curves, respectively, as functions of **k** along the edges of the Brillouin zone. Shaded areas indicate the band gaps. (For interpretation of the references to colour in this figure legend, the reader is referred to the web version of this article.)

We set the lattice parameter in the undeformed configuration to 6.3 mm and consider two values of the prescribed electric field, namely $e = 150$ MV/m and $e = 300$ MV/m.

To appreciate the results obtained by the optimization process of the unit cell, we provide first as a comparison the results for the standard unit cell of a central circular fiber, when optimized over all fiber volume fractions (Shmuel, 2013). At $e = 150$ MV/m, the width of the widest gap is 1.05 kHz, obtained using a volume fraction of 0.68. The greatest relative change obtained via the electric actuation is 5.56%. At $e = 300$ MV/m, the width of the widest gap is 1.13 kHz, obtained using a volume fraction of 0.69. The greatest relative change obtained via the electric actuation is 32.36%.

We begin by assuming a symmetric unit cell and employing the pixel grid representation. Using this representation, the number of design variables is 100, and the number of possible unit cells is 3.6×10^{16}. The genetic algorithm evaluated 12,500 unit cells until convergence. Unit cells that optimize the gap width and its relative change are depicted in the left panels of Figs. 6 and 7, respectively. The first and second rows in each Fig. correspond to $e = 150$ MV/m and 300 MV/m, respectively. Right panels show the corresponding band diagrams. Specifically, the eigenfrequencies in the reference and in the actuated configuration are shown by continuous red and dashed blue curves, respectively, as functions of **k** along the edges of the Brillouin zone. Left- and right-hatched areas indicate band gaps in the actuated and reference states, respectively.

The fiber volume fraction in Fig. 6(a) is 0.64, achieving a maximal gap width of 4.05 kHz at $e = 150$ MV/m. The fiber volume fraction in Fig. 6(b) is also 0.64, achieving a maximal gap width of 4.31 kHz at $e = 300$ MV/m.

The fiber volume fraction in Fig. 7(a) is 0.55, achieving a relative change of 5.81% at $e = 150$ MV/m. The fiber volume fraction in Fig. 7(b) is 0.59, achieving a relative change of 43.09% at $e = 300$ MV/m.

Next, we relax the symmetry constraint on the unit cell and employ a closed spline with four control points to model a single fiber inclusion, such that corresponding number of design variables is 8. The reduction in the number of design variables led to a significant reduction in computation times, and the genetic algorithm evaluated 7500 unit cell until convergence. We recall that by using a single spline, our design space comprises only unit cells with a single inclusion and interface. We further recall that the gaps emerge from the interference of incident and secondary waves that are scattered across interfaces. Accordingly, we *a priori* expect that optimized unit cells with a single inclusion and interface will be inferior to optimized unit cells with multiple inclusions and interfaces.

Proceeding to the results, we illustrate the optimized unit cells using the single spline representation with respect to the gap width and its relative change in the left panels of Figs. 6–9, respectively. Again, the first and second rows in each Fig. correspond to $e = 150$ MV/m and 300 MV/m, respectively. Right panels show the corresponding band diagrams, with the same notation of the previous Figs.

The fiber volume fraction in Fig. 8(a) is 0.65, achieving a maximal gap width of 1.43 kHz at $e = 150$ MV/m. The fiber volume fraction in Fig. 8(b) is 0.69, achieving a maximal gap width of 1.67 kHz at $e = 300$ MV/m.

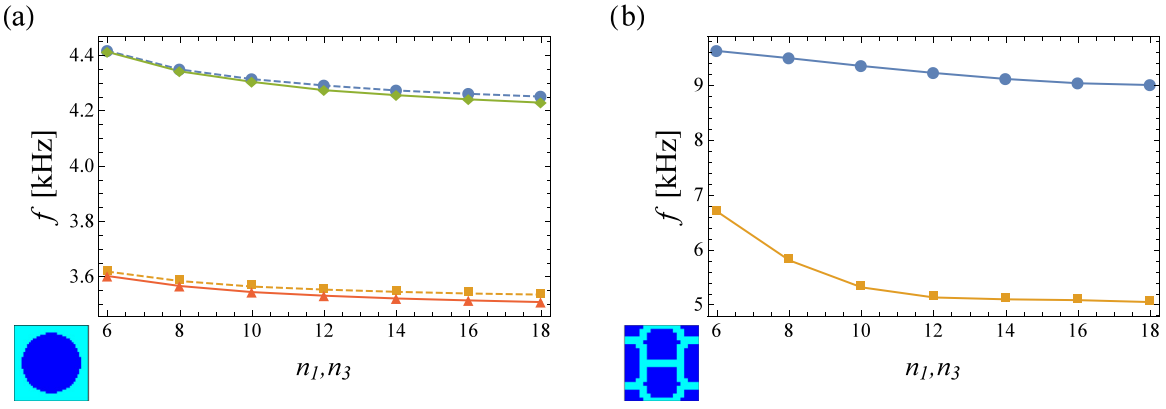

Fig. 11. Upper and lower frequencies of the maximum band gap are as functions of n_1 and n_3. Panels a) and b) correspond to the circular fiber in Fig. 10, and a representative optimized cell, respectively. In panel a) solid and dashed lines denoting the PWE and FPWE methods, respectively.

Table 2
Objective functions of a unit cell with circular fiber of optimal volume fraction, and genetic algorithm-based unit cells represented using pixel grid and B-spline.

	Maximal width			Greatest relative change		
	Circular	Pixel grid	B-spline	Circular	Pixel grid	B-spline
$e = 150$ MV/m	1.05 kHz	4.05 kHz	1.43 kHz	5.56%	5.81%	5.76%
$e = 300$ MV/m	1.13 kHz	4.31 kHz	1.67 kHz	32.36%	43.09%	32.46%

The fiber volume fraction in Fig. 9(a) is 0.6, achieving a relative change of 5.76% at $e = 150$ MV/m. The fiber volume fraction in Fig. 9(b) is 0.65, achieving a relative change of 32.46% at $e = 300$ MV/m. The results of the optimization process are summarized in Table 2.

6. Conclusions

In Section 4, we introduced a scheme to optimize dielectric elastomer fiber composites for wide band gaps, which are tunable via electrostatically-controlled nonlinear deformations. This topology optimization was applied to a case study of anti-plane shear waves in specific pre-deformed composites across the audible frequency range, however it is extensible to more general settings, *i.e.*, in-plane waves of general propagation direction, three-dimensional compressible composites, and pre-deformations that maintain the composite periodicity. The optimization objective is to maximize the gap width associated with the actuated state, or the relative change in the gap width between actuated and unactuated states, at prescribed electric fields.

Two approaches for the representation of the unit cell have been employed. The first one is based on the pixel grid only, where the design variables are given by the components of the material distribution bit-string. The second one is based on the projection of a closed B-spline onto the pixel grid, where the number of design variables is reduced to the number of the coordinates of the B-spline control points.

Optimization results summarized in Table 2 were obtained using two different representations for the design variables, namely, pixel grid and B-spline. Assuming symmetric unit cells to reduce the number of design variables, pixel grid-based optimization demonstrated a significant increase in the gap width with respect to a unit cell with an optimal circular fiber. An improvement in the relative change of the gap width was also demonstrated, albeit very moderate. These improvements can be made more significant by relaxing the symmetry restriction and increasing the number of pixels, at the cost of longer computation times. Optimization results based on the four point B-spline representation, which uses a significantly smaller number of design variables (8 versus 100), also demonstrated improvement with respect to a unit cell with an optimal circular fiber, however not substantial enough. This performance can be improved by increasing the design space via (i) additional splines; (ii) additional control points for each spline, and (iii) a higher number of pixels.

Acknowledgments

GS and EB acknowledge the support of the Israel Science Foundation, founded by the Israel Academy of Sciences and Humanities (grant no. 1912/15). The work of EB at Technion has been supported in part by the Lady Davis Foundation fellowship. The authors wish to thank Yosef Yoely for providing parts of the code for B-spline optimization.

Appendix

The standard plane wave expansion (PWE) method is a popular technique to calculate different band diagrams, namely, in quantum mechanics, optics, and particularly for elastic composites (*e.g.*, Kushwaha et al., 1993; Sigalas and Economou, 1996; Vasseur et al., 2002; Barnwell et al., 2017), owing to its simplicity and the fact that it is exact, as the Fourier functions constitute a complete basis for solution. Several experimental works agree with its predictions (*e.g.*, Vasseur et al., 2002; Pichard et al., 2012), and investigations on its convergence rate conclude that it depends on the specific formulation and contrast between the phase properties (*e.g.*, Cao et al., 2004; Tanaka et al., 2000). To the best of our knowledge, except the work of Xie et al. (2017), a corresponding analysis of the FPWE method is not available; accordingly, we carried out the following investigation. Firstly, we tested the FPWE using two benchmark problems, namely, circular and square fibers at the center of the unit cell, in order to check if the solutions agree with the solutions obtained via the PWE method. The case of the square fiber is reported also by Xie et al. (2017), therein a comparison of the FPWE method with the finite element method is provided. Our investigation of the circular fiber case is given in Fig. 10, providing a comparison of the band structures obtained via PWE and FPWE methods, where the latter was carried out using a pixelation of 40×40 grid. Therein, eigenfrequencies obtained by employing the PWE and FPWE methods are shown by solid blue and dashed red curves, respectively, demonstrating good agreement. Specifically, the error in the gap size is approximately 1%. Secondly, we examined the dependency on the number of plane waves by evaluating the gap range as function of the indices n_1, n_3, which determine the number plane waves (indices 6, 8, 10, 12, 14, 16, and 18 correspond to 169, 289, 441, 625, 841, 1089 and 1369 plane waves, respectively). Our investigation for the circular fiber and representative optimized unit cell is given in Fig. 11. Therein, results obtained using the PWE and FPWE methods for the circular fiber are given by solid and dashed lines, respectively. We find that 441 plane waves is a good compromise between computational time and accuracy, as with this number, the difference in the gap width is 5% in comparison with 1369 plane waves. Accordingly, this is the number we used throughout our computations.

References

Babaee, S., Viard, N., Wang, P., Fang, N.X., Bertoldi, K., 2016. Harnessing deformation to switch on and off the propagation of sound. Adv. Mater. 8, 1631–1635.

Barnwell, E.G., Parnell, W.J., Abrahams, I.D., 2017. Tunable elastodynamic band gaps. Extreme Mech. Lett. 12, 23–29. doi:10.1016/j.eml.2016.10.009. ISSN 2352-4316 http://www.sciencedirect.com/science/article/pii/S2352431616300815. Frontiers in Mechanical Metamaterials

Bayat, A., Gordaninejad, F., 2015. Band-gap of a soft magnetorheological phononic crystal. J. Vib. Acoust. Trans. ASME 137 (1), 011011. doi:10.1115/1.4028556.

Bendsøe, M.P., Kikuchi, N., 1988. Generating optimal topologies in structural design using a homogenization method. Comput. Methods Appl. Mech. Eng. 71 (2), 197–224. doi:10.1016/0045-7825(88)90086-2. ISSN 0045-7825. http://www.sciencedirect.com/science/article/pii/0045782588900862

Bendsøe, M.P.B., Sigmund, O., 2003. Topology Optimization: Theory, Methods, and Applications. In: Engineering Online Library. Springer Berlin Heidelberg. ISBN 9783540429920. URL https://books.google.co.il/books?id=NGmtmMhVe2sC

Bilal, O.R., Hussein, M.I., 2011. Ultrawide phononic band gap for combined in-plane and out-of-plane waves. Phys. Rev. E 84, 065701. doi:10.1103/PhysRevE.84.065701.

Bortot, E., Shmuel, G., 2017. Tuning sound with soft dielectrics. Smart Mater. Struct. 26, 045028. doi:10.1088/1361-665X/aa6387.

Cao, Y., Hou, Z., Liu, Y., 2004. Convergence problem of plane-wave expansion method for phononic crystals. Phys. Lett. A 327 (2), 247–253. doi:10.1016/j.physleta.2004.05.030.

Carpi, F., De Rossi, D., Kornbluh, R., Pelrine, R., Sommer-Larsen, P., 2008. Dielectric Elastomers as Electromechanical Transducers: Fundamentals, Materials, Devices, Models and Applications of an Emerging Electroactive Polymer Technology. Elsevier Science. ISBN 978-0-08-047488-5

Celli, P., Gonella, S., Tajeddin, V., Muliana, A., Ahmed, S., Ounaies, Z., 2017. Wave control through soft microstructural curling: bandgap shifting, reconfigurable anisotropy and switchable chirality. Smart Mater. Struct. 26 (3), 035001. URL http://stacks.iop.org/0964-1726/26/i=3/a=035001

Craster, R.V., Antonakakis, T., Makwana, M., Guenneau, S., 2012. Dangers of using the edges of the brillouin zone. Phys. Rev. B 86, 115130. doi:10.1103/PhysRevB.86.115130. URL http://link.aps.org/doi/10.1103/PhysRevB.86.115130

Degraeve, S., Granger, C., Dubus, B., Vasseur, J.O., Thi, M.P., Hladky, A.C., 2015. Tunability of bragg band gaps in one-dimensional piezoelectric phononic crystals using external capacitances. Smart Mater. Struct. 24 (8), 085013. URL http://stacks.iop.org/0964-1726/24/i=8/a=085013

Dorfmann, A., Ogden, R.W., 2005. Nonlinear electroelasticity. Acta Mech. 174, 167–183.

Dorfmann, A., Ogden, R.W., 2010. Nonlinear electroelastostatics: incremental equations and stability. Int. J. Eng. Sci. 48 (1), 1–14. doi:10.1016/j.ijengsci.2008.06.005. ISSN 0020-7225. URL http://www.sciencedirect.com/science/article/pii/S0020722508001043

Gazonas, G.A., Weile, D.S., Wildman, R., Mohan, A., 2006. Genetic algorithm optimization of phononic bandgap structures. Int. J. Solids Struct. 43 (18–19), 5851–5866. doi:10.1016/j.ijsolstr.2005.12.002.

Gei, M., Roccabianca, S., Bacca, M., 2011. Controlling bandgap in electroactive polymer-based structures. IEEE-ASME Trans. Mechatron. 16, 102–107.

Getz, R., Kochmann, D.M., Shmuel, G., 2017. Voltage-controlled complete stopbands in two-dimensional soft dielectrics. Int. J. Solids Struct. 113–114, 24–36. doi:10.1016/j.ijsolstr.2016.10.002. ISSN 0020-7683. URL http://www.sciencedirect.com/science/article/pii/S0020768316302931

Getz, R., Shmuel, G., 2017. Band gap tunability in deformable dielectric composite plates. Int. J. Solids Struct. 128, 11–22. doi:10.1016/j.ijsolstr.2017.07.021. ISSN 0020-7683. URL http://www.sciencedirect.com/science/article/pii/S0020768317303384

Godaba, H., Foo, C.C., Zhang, Z.Q., Khoo, B.C., Zhu, J., 2014. Giant voltage-induced deformation of a dielectric elastomer under a constant pressure. Appl. Phys. Lett. 105 (11), 112901. doi:10.1063/1.48958151.

Halkjær, O., Sigmund, S., Jensen, J.S., 2006. Maximizing band gaps in plate structures. Struct. Multidiscip. Optim. 32 (4), 263–275. doi:10.1007/s00158-006-0037-7.

Hedayatrasa, S., Abhary, K., Uddin, M.S., Guest, J.K., 2016. Optimal design of tunable phononic bandgap plates under equibiaxial stretch. Smart Mater. Struct. 25, 055025. doi:10.1088/0964-1726/25/5/055025.

Holland, J.H., 1992. Genetic algorithms. Sci. Am. 267 (7), 66–72. doi:10.1038/scientificamerican0792-66.

Huang, J., Li, T., Foo, C.C., Zhu, J., Clarke, D.R., Suo, Z., 2012. Giant, voltage-actuated deformation of a dielectric elastomer under dead load. Appl. Phys. Lett. 100 (4). doi:10.1063/1.3680591. ISSN 0003-6951

Hussein, M.I., Hamza, K., Hulbert, G.M., Saitou, K., 2007. Optimal synthesis of 2d phononic crystals for broadband frequency isolation. Waves Random Complex Media 17 (4), 491–510. doi:10.1080/17455030701501869.

Hussein, M.I., Leamy, M.J., Ruzzene, M., 2014. Dynamics of phononic materials and structures: historical origins, recent progress, and future outlook. Appl. Mech. Rev. 66 (4). 040802–040802 URL https://doi.org/10.1115/1.4026911

Jia, K., Wang, M., Lu, T., Zhang, J., Wang, T., 2016. Band-gap tunable dielectric elastomer filter for low frequency noise. Smart Mater. Struct. 25 (5), 055047. URL http://stacks.iop.org/0964-1726/25/i=5/a=055047

Kittel, C., 2005. Introduction to Solid State Physics. John Wiley & Sons, Inc., Hoboken, NJ.

Kushwaha, M.S., Halevi, P., Dobrzynski, L., Djafari-Rouhani, B., 1993. Acoustic band structure of periodic elastic composites. Phys. Rev. Lett. 71 (13), 2022–2025.

Li, T., Keplinger, C., Baumgartner, R., Bauer, S., Yang, W., Suo, Z., 2013. Giant voltage-induced deformation in dielectric elastomers near the verge of snap-through instability. J. Mech. Phys. Solids 61 (2), 611–628.

Li, Y.F., Huang, X., Meng, F., Zhou, S., 2016. Evolutionary topological design for phononic band gap crystals. Struct. Multidiscip. Optim. 54 (3), 595–617. doi:10.1007/s00158-016-1424-3.

Liu, Z.F., Wu, B., He, C.F., 2014. Band-gap optimization of two-dimensional phononic crystals based on genetic algorithm and FPWE. Waves Random Complex Media 24 (3), 286–305. doi:10.1080/17455030.2014.901582.

Liu, Z.F., Wu, B., He, C.F., 2016. Systematic topology optimization of solid-solid phononic crystals for multiple separate band-gaps with different polarizations. Ultrasonics 65, 249–257. doi:10.1016/j.ultras.2015.09.017.

Lu, Y., Yang, Y., Guest, J.K., Srivastava, A., 2017. 3-D phononic crystals with ultra-wide band gaps. Sci. Rep. 7 (43407). EP –, 02 URL https://doi.org/10.1038/srep43407

McMeeking, R.M., Landis, C.M., 2005. Electrostatic forces and stored energy for deformable dielectric materials. J. Appl. Mech. 72, 581–590.

Meng, F., Li, Y., Li, S., Lin, H., Jia, B., Huang, X., 2017. Achieving large band gaps in 2d symmetric and asymmetric photonic crystals. J. Lightwave Technol. 35 (9), 1670–1676. doi:10.1109/JLT.2017.2667681.

Pelrine, R., Kornbluh, R., Pei, Q.B., Joseph, J., 2000. High-speed electrically actuated elastomers with strain greater than 100%. Science 287, 836–839.

Pichard, H., Richoux, O., Groby, J.P., 2012. Experimental demonstrations in audible frequency range of band gap tunability and negative refraction in two-dimensional sonic crystal. J. Acoust. Soc. Am. 132 (4). doi:10.1121/1.4744974.

Ruzzene, M., Baz, A., 1999. Control of wave propagation in periodic composite rods using shape memory inserts. J. Vib. Acoust. 122 (2), 151–159. URL https://doi.org/10.1115/1.568452

Shmuel, G., 2013. Electrostatically tunable band gaps in finitely extensible dielectric elastomer fiber composites. Int. J. Solids Struct. 50 (5), 680–686.

Shmuel, G., Band, R., 2016. Universality of the frequency spectrum of laminates. J. Mech. Phys. Solids 92, 127–136. doi:10.1016/j.jmps.2016.04.001. ISSN 0022-5096

Shmuel, G., deBotton, G., 2012. Band-gaps in electrostatically controlled dielectric laminates subjected to incremental shear motions. J. Mech. Phys. Solids 60, 1970–1981.

Shmuel, G., Pernas-Salomón, R., 2016. Manipulating motions of elastomer films by electrostatically-controlled aperiodicity. Smart Mater. Struct. 25 (12), 125012. URL http://stacks.iop.org/0964-1726/25/i=12/a=125012

Sigalas, M.M., Economou, E.N., 1992. Elastic and acoustic wave band structure. J. Sound Vib. 158 (2), 377–382.

Sigalas, M.M., Economou, E.N., 1996. Attenuation of multiple scattered sound. Europhys. Lett. 36, 241.

Sigmund, O., Jensen, J.S., 2003. Systematic design of phononic band–gap materials and structures by topology optimization. Philos. Trans. R. Soc. Lond. A 361 (1806), 1001–1019. doi:10.1098/rsta.2003.1177.

Srivastava, A., 2016. Metamaterial properties of periodic laminates. J. Mech. Phys. Solids 96, 252–263. doi:10.1016/j.jmps.2016.07.018. ISSN 0022-5096. URL http://www.sciencedirect.com/science/article/pii/S0022509616303933

Suo, Z., Zhao, X., Greene, W.H., 2008. A nonlinear field theory of deformable dielectrics. J. Mech. Phys. Solids 56 (2), 467–486.

Tanaka, Y., Tomoyasu, Y., Tamura, S.I., 2000. Band structure of acoustic waves in phononic lattices: Two-dimensional composites with large acoustic mismatch. Physical Review B 62 (11), 7387–7392.

Tian, L., Tevet-Deree, L., deBotton, G., Bhattacharya, K., 2012. Dielectric elastomer composites. J. Mech. Phys. Solids 60, 181–198.

Vasseur, J.O., Deymier, P.A., Khelif, A., Lambin, P., Djafari-Rouhani, B., Akjouj, A., Dobrzynski, L., Fettouhi, N., Zemmouri, J., 2002. Phononic crystal with low filling fraction and absolute acoustic band gap in the audible frequency range: a theoretical and experimental study. Phys. Rev. E 65 (5), 056608. doi:10.1103/PhysRevE.65.056608.

Vondřejc, J., Rohan, E., Heczko, J., 2017. Shape optimization of phononic band gap structures using the homogenization approach. Int. J. Solids Struct. 113, 147–168. doi:10.1016/j.ijsolstr.2017.01.038.

Wen, J., Wang, G., Yu, D., Zhao, H., Liu, Y., 2005. Theoretical and experimental investigation of flexural wave propagation in straight beams with periodic structures: application to a vibration isolation structure. J. Appl. Phys. 97 (11), 114907. doi:10.1063/1.1922068. URL http://scitation.aip.org/content/aip/journal/jap/97/11/10.1063/1.1922068

Xie, L., Xia, B., Liu, J., Huang, G., Lei, J., 2017. An improved fast plane wave expansion method for topology optimization of phononic crystals. Int. J. Mech. Sci. 120, 171–181. doi:10.1016/j.ijmecsci.2016.11.023.

Yi, G., Youn, B.D., 2016. A comprehensive survey on topology optimization of phononic crystals. Struct. Multidiscip. Optim. 54 (5), 1315–1344. doi:10.1007/s00158-016-1520-4.

Yin, J., Peng, H.J., Zhang, S., Zhang, H.W., Chen, B.S., 2015. Design of nacreous composite material for vibration isolation based on band gap manipulation. Comput. Mater. Sci. 102, 126–134. doi:10.1016/j.commatsci.2015.01.032. ISSN 0927-0256. URL http://www.sciencedirect.com/science/article/pii/S0927025615000397

Yu, X., Lu, Z., Cui, F., Cheng, L., Cui, Y., 2017. Tunable acoustic metamaterial with an array of resonators actuated by dielectric elastomer. Extreme Mech. Lett. 12, 37–40. doi:10.1016/j.eml.2016.07.003. ISSN 2352-4316. URL http://www.sciencedirect.com/science/article/pii/S2352431616300414. Frontiers in Mechanical Metamaterials

Zelhofer, A.J., Kochmann, D.M., 2017. On acoustic wave beaming in two-dimensional structural lattices. Int. J. Solids Struct. 115–116, 248–269. doi:10.1016/j.ijsolstr.2017.03.024. ISSN 0020-7683. URL http://www.sciencedirect.com/science/article/pii/S0020768317301336

Ziser, Y., Shmuel, G., 2017. Experimental slowing of flexural waves in dielectric elastomer films by voltage. Mech. Res. Commun. 85, 64–68. doi:10.1016/j.mechrescom.2017.08.005.